

Activated carbons prepared by hydrothermal pretreatment and chemical activation of *Eucommia ulmoides* wood for supercapacitors application

Guotao Sun, Ling Qiu, Mingqiang Zhu*, Kang Kang, Xiaohui Guo

Department of Agricultural Engineering, Northwest A&F University, Yangling 712100, China

ARTICLE INFO

Keywords:

Eucommia ulmoides Oliver
Activated carbon
Supercapacitor
Hydrothermal pretreatment
Specific capacitance

ABSTRACT

Eucommia ulmoides Oliver (EUO) wood goes through hydrothermal pretreatment (HTP) followed by chemical activation to produce activated carbons (ACs), which are then applied as electrode materials for supercapacitors application. The porous structure, surface chemistry and electrochemical characteristics of the ACs have been investigated in detail. The specific surface area (S_{BET}) of the ACs enlarges from 1272.38 to 1534.06 $\text{m}^2 \text{g}^{-1}$ following the increase of HTP temperature from 150 to 170 °C, and then decreases to 1284.69 $\text{m}^2 \text{g}^{-1}$ when HTP temperature increased further to 200 °C, indicating that HTP temperature of 170 °C is the turning point on S_{BET} of the ACs. Moreover, the ACs obtained at HTP temperature of 170 °C are observed with highest mesopore pore volume (1.66 $\text{cm}^3 \text{g}^{-1}$) and mesopore pore diameter (6.02 nm). Additionally, the Raman and FTIR spectrum of the ACs also prove that HTP temperature of 170 °C can enhance the graphitization during the activation process, indicated with low $I_{\text{D}}/I_{\text{G}}$ ratio (0.74) and vibrational amplitude. These results reveal that the HTP effectively influences the porous structure and surface chemistry characteristics of the ACs by manipulating substrate structure of the ACs precursor. The characterization of the porous structure and surface chemistry illustrate that the activated carbon produced via HTP at 170 °C for 1 h exhibited high specific surface area (1456.69 $\text{m}^2 \text{g}^{-1}$) along with large percentage of mesopores pore volume (93%), which then result in high specific capacitance of 185 Fg^{-1} and long-term cycling performance. This study prove that the EUO derived ACs are promising materials for supercapacitor application and can expand EUO wood for feasible application in supercapacitors.

1. Introduction

The urgency to seek a more attractive and sustainable energy storage device has become clear with increasing global energy demand, the finite fossil fuel reserves, and excessive exhaust gas emissions (Karnan et al., 2017). As a promising energy storage device, the electrochemical supercapacitors possess the advantages of exceptional cycling performance and fast charge-discharge rate with relatively high power density comparing to the traditional batteries and capacitors (Borenstein et al., 2017; Liu et al., 2015; Stoller and Ruoff, 2010), which makes it a research hotspot in recent years. However, the bottleneck that limiting its large-scale application is the low energy density (Yin et al., 2016).

On the basis of the electrode materials used, supercapacitors can be broadly categorized into carbon-based supercapacitors, metal oxide

based supercapacitors and conducting polymer-based supercapacitors (Barzegar et al., 2017). Though, the metal oxide and conducting polymer based supercapacitors can supply higher specific capacitance than carbon-based supercapacitor, the dependence on expensive metal resources and poor cycling stability limits its wide application (Chiam et al., 2017; Potphode et al., 2017). In contrast, carbon-based supercapacitors have better application potential than pseudocapacitors because of the high electrochemical cyclability, cost competitiveness and natural abundance (Beidaghi and Gogotsi, 2014; Boyjoo et al., 2017; Li et al., 2016; Wang et al., 2016). Recently, the non-aqueous electrolyte like organic and ionic liquid have been studied to improve the working voltage of the supercapacitors (Karnan et al., 2017), but the poor ion diffusion of the non-aqueous electrolyte limits its wide application due to the low mesoporosity (Ohno and Fukumoto, 2008). In this perspective, the preparation of the targeted carbon materials with desirable

Abbreviations: EUO, *Eucommia ulmoides* Oliver; HTP, hydrothermal pretreatment; ACs, activated carbons; FTIR, Fourier transform infrared spectroscopy; EUOACs, *Eucommia ulmoides* Oliver derived activated carbons; XRD, X-ray diffraction; CHNS, carbon, hydrogen, nitrogen and sulfur; BET, Brunauer, Emmett and Teller; CV, cyclic voltammetry; EIS, electrochemical impedance spectroscopy; GCD, galvanic charge and discharge; EUOBCs, *Eucommia ulmoides* Oliver derived biochars; SEM, scanning electron microscope; PSD, pore size distribution; EDLC, double layer capacitance; DC, discharge capacitance; IR, internal resistance

* Corresponding author.

E-mail address: zmqsx@nwsuaf.edu.cn (M. Zhu).

<https://doi.org/10.1016/j.indcrop.2018.08.082>

Received 3 June 2018; Received in revised form 24 August 2018; Accepted 30 August 2018

Available online 05 September 2018

0926-6690/ © 2018 Published by Elsevier B.V.

composite structure of micropores and mesopores is indispensable for supercapacitors application.

Various carbon-based nanostructured materials such as graphene (Lee et al., 2017), carbon nanosheets (Sodtipinta et al., 2017), carbon fiber (Yang et al., 2018) and carbon aerogel (Zhuo et al., 2016) have been intensively studied as electrode active materials for supercapacitors. However, most of these materials still suffer from the harsh preparation process due to the complexity of the preparation procedure and high cost. Recently, the utilization of sustainable biomass-derived activated carbons (ACs) materials as electrode materials for supercapacitors have drawn wide attention due to their natural abundance, high surface area, easy preparation procedure, and low cost (Ahmad and Danish, 2018; Danish et al., 2017; Ma et al., 2015; Tan et al., 2017; Tang et al., 2018). A wide diversity of biomass that have been studied for supercapacitors application with improved specific capacitance and energy density include hemp (Sun et al., 2016), bean dregs (Teng et al., 2016), prawn shell (Gao et al., 2016), cotton stalk (Tian et al., 2017), corn grain (Qu et al., 2015), rice husk (Zhang et al., 2017), banana peels (Zhang et al., 2016) and olive pits (Redondo et al., 2015). The main component of these lignocellulosic biomass are cellulose, hemicellulose and lignin, and the amount of these components varies with respect to different plant species (Zhu et al., 2017). The chemical activation of the biomass components can form porous carbon materials with large specific surface area and desirable micro- and meso- porous structure. Guo and Rockstraw (2006) reported that the yield of the activated carbon from hemicellulose is lower than that from cellulose and lignin when prepared under the same activation conditions, and the hemicellulose-derived activated carbon gain lower specific surface area. The main reason is that hemicellulose was decomposed into gas and volatile fraction during the activation process (Bouchelta et al., 2008; Jain et al., 2015), which significantly impacts the chemical activation process (Hao et al., 2017). The observation further suggests that the chemical composition of the substrate could affect the porous characteristics of the resulted activated carbons and the modification of the hemicellulose by a pretreatment step before activation process may improve its porous structure. To better understand the variation tendency of chemical composition during pretreatment process, it is critical to investigate the effect of the pretreatment on the chemical characteristics of the substrate under different conditions.

Hydrothermal pretreatment (HTP) has been applied to improve the porous characteristics of the resulted ACs. Hardwood derived ACs achieved higher surface area of $2143 \text{ m}^2 \text{ g}^{-1}$ with HTP at 150°C for 100 min. than the treatment in absence of HTP ($1799 \text{ m}^2 \text{ g}^{-1}$) (Yagmur et al., 2013). Xiao et al., (2017) reported that the specific surface area of glucose derived mesoporous carbon was improved from 390 to $520 \text{ m}^2 \text{ g}^{-1}$ by using hydrothermal pretreatment (180°C for 1 day) followed by thermal treatment (600°C for 3 h). A HTP process at 200°C for 90 min resulted in higher surface area of the lignite derived activated carbon ($3069 \text{ m}^2 \text{ g}^{-1}$) than that from direct activation of the lignite ($2239 \text{ m}^2 \text{ g}^{-1}$) (Yu et al., 2015). In short, HTP is an effective, cost competitive and environmental friendly procedure to modify the chemical characteristics of the ACs precursor, which then resulted in the formation of the ACs with better porous structure for further application. Above all, it is vital to investigate the effect of HTP on the porous characteristics of activated carbons and the corresponding electrochemical performance.

Eucommia ulmoides Oliver (EUO), named as Dù-zhòng (in Chinese), is natively planted in China for harvesting the leaves and bark as special Chinese herb (Ji and Su, 2006). However, the research on the high-value utilization of branch wood has rarely been reported. Therefore, the conversion of the huge amount of branch wood into value-added materials can significantly increase the economic value of the EUO.

In this study, HTP followed by chemical activation process was applied to convert *Eucommia ulmoides* Oliver (EUO) wood into ACs. The amorphous nature of ACs was characterized by using XRD, FT-IR, Raman, CHNS and BET analysis, and the electrochemical performance

of the ACs was studied via CV, EIS, and GCD analysis. The effect of different HTP temperatures and retention time on the properties of the ACs and the corresponding capacitive performance was investigated to illuminate the correlation of the porous structure and electrochemical characteristics of the ACs.

2. Materials and methods

2.1. Preparation of the EUO-derived ACs

The EUO wood used for synthesis of the activated carbons were harvested from an experimental field of Northwest A&F University (Yangling, China). After removal of the bark and leaves, the EUO chips were used to prepare activated carbons via hydrothermal pretreatment followed by chemical activation. The detailed procedures were described in previously published paper by Zhu et al., (2017). The EUO chips were ground, dewaxed and dried before the hydrothermal treatment which is conducted in 1000 mL stainless steel autoclave with sparging nitrogen gas. The dewaxed EUO chips (40.0 g), which were mixed with at solid to liquid ratio of 1:10 (g/mL), were autoclaved at 150 , 160 and 170°C for 1.0 h, and 170 , 180 , 190 and 200°C for 0.5 h, respectively. The deionized water used in this study was prepared by a Milipore (Moll-1810b, Chongqing molwater co. LTD). After the reaction, the hydrothermal residues were filtrated and dried overnight at 60°C in oven to obtain the biochars. The biochars were labelled as EUOBC₁ (150°C for 1.0 h), EUOBC₂ (160°C for 1.0 h), EUOBC₃ (170°C for 1.0 h), EUOBC₄ (170°C for 0.5 h), EUOBC₅ (180°C for 0.5 h), EUOBC₆ (190°C for 0.5 h), and EUOBC₇ (200°C for 0.5 h), respectively. In order to investigate the effect of the HTP the characteristics of the biochars, the EUO wood without hydrothermal treatment was set as control group and labeled as EUOBC₀. The chemical activation of the EUOBCs was performed in a rotary tube furnace with maximum heating temperature of 1200°C (OTF-1200X-R). The EUOBCs (10.0 g) were mixed with 50 mL of 50 wt% phosphoric acid and then heated up to 550°C at a rate of $5^\circ \text{C}/\text{min}$ under a N_2 flow ($10 \text{ mL}/\text{min}$) atmosphere, and the mixture was chemically activated at 550°C for 2 h. Next, the activated samples were washed with hot distilled water until the pH value of the filtrate reach 7.0. Afterward, the washed activated carbons (ACs) were dried at 110°C for 12 h and named as EUOAC₀, EUOAC₁, EUOAC₂, EUOAC₃, EUOAC₄, EUOAC₅, EUOAC₆ and EUOAC₇, respectively. All the EUOACs were transferred into a shearing grinding mill (M20, IKA, Germany) and processed at 20,000 rpm for 3 min. Then the milled EUOACs were ready for further analysis of porosity characteristics and surface chemistry.

2.2. Characterization of the EUO-derived ACs

To determine the pore features and surface area of the ACs, the Nitrogen adsorption/desorption isotherms, BET and BJH of the substrates were detected using a V-Sorb 2800 P surface area analyzer (Gold APP Instruments Corporation, Beijing, China). The surface area and porosity properties of the substrates were determined by nitrogen (N_2) adsorption-desorption at -196°C (77 K), and the samples were degassed at 150°C for 12 h under vacuum to clean the surface. The Brunauer-Emmett-Teller (BET) surface area was assessed within the range of relative pressures from 0.05 to 0.3. The Barrett-Joyner-Halenda (BJH) method was used in the average pore width and pore size distribution determination. The elemental composition of ACs were measured by elemental analyzer (Vario Macro Cube, Elementar, Germany) working under CHNS mode. The X-ray diffraction patterns were measured by a Bruker D8 advance X-ray diffractometer with a $\text{Cu K}\alpha$ radiation ($\lambda = 0.15418 \text{ nm}$) in 2θ range from 10° to 80° . The surface morphological features of the EUOACs were analyzed by a scanning electron microscope (SEM) (TM 3030, Hitachi, Japan) and a transmission electron microscopy (HT7700, Hitachi, Japan). A Raman microscope (Horiba JobinYvon, Longjumeau, France) was used to

measure the Raman spectra of the ACs. Fourier transform infrared spectroscopy (FT-IR) measurement was performed using a spectrophotometer (Nicolet iN10, Thermo Scientific, USA). All the experiments were conducted in duplicate, and the results were average values.

2.3. Electrode preparation and electrochemical measurements

The Electrode materials were fabricated by mixing 85 wt% of EUOACs, 10 wt% carbon black (SUPER-P, TIMCAL) and 5 wt% of polytetrafluoroethylene (PTFE, ALDRICH) and rolling into thin film. Then, the mixed films were coated on stainless steel mesh and dried at 80 °C overnight to form the electrodes which served as working electrode with active materials loading of ~2 mg.

The electrochemical performance of the EUOAC₀, EUOAC₁, EUOAC₂, EUOAC₃, EUOAC₄, EUOAC₅, EUOAC₆ and EUOAC₇ was studied by cyclic voltammetry (CV), electrochemical impedance spectroscopy (EIS), and galvanostatic charge-discharge (GCD) analysis. All the CV experiments were conducted in a three-electrode system operated on an electrochemical working station (CHI660E, Shanghai, China). In this three-electrode system, the platinum foil was applied as the counter electrode and the Hg/Hg₂SO₄ electrode served as the reference electrode. The potential window was ranged from −0.8 to +0.4 V using 1 M H₂SO₄ as the electrolyte. The EIS data was collected by using electrochemical workstation (CHI660E, Shanghai, China) with the frequency range from 100 kHz to 10 mHz and an AC signal amplitude of 5 mV at open circuit potential. GCD experiments were carried out by a battery test system (CT-4008, Neware, China) with charging-discharging current densities ranging from 0.2 to 2 Ag^{−1}.

From the CV curves the specific capacitance of the electrodes were calculated by using following equation (Yin et al., 2016):

$$C_{sc} = \frac{Q}{2\Delta Vm} \quad (1)$$

Where C_{sc} (Fg^{−1}) is the specific capacitance of the active materials, $Q/2$ is the half of integration area of CV curves, ΔV is the potential window of the CV curves and m is the mass of the active materials. According to the EIS test, the real specific capacitance and imaginary capacitance can be calculated by following equations (Yin et al., 2016):

$$C' = \frac{-Z(\omega)''}{m\omega |Z(\omega)|^2} \quad (2)$$

$$C'' = \frac{-Z(\omega)'}{m\omega |Z(\omega)|^2} \quad (3)$$

Where C' is the real specific capacitance, C'' is the imaginary specific capacitance, $Z(\omega)''$ is the imaginary impedance, $Z(\omega)'$ is the real impedance, $Z(\omega)$ is the impedance, and m is the mass of the active materials. For GCD analysis, the discharge capacitance can be calculated based on the following equation (Stoller and Ruoff, 2010):

$$C_{dc} = \frac{i\Delta t}{(V_2 - iR - V_1)} \quad (4)$$

Where C_{dc} is the discharge capacitance of the active materials, V_2 is the high potential of the voltage window, V_1 is the low potential of the voltage window, and iR is the voltage drop of V_2 at discharge start.

3. Results and discussion

3.1. Characteristics of the porous structure of EUOACs

In this study, the EUOACs were prepared by hydrothermal pretreatment (HTP) of EUO wood under different temperatures (range from 150 °C to 200 °C) and retention times (0.5, 1 h), and followed by H₃PO₄ (50 wt%) activation at 550 °C for 2 h. Table 1 lists the content of cellulose, hemicellulose and lignin of the EUOACs after HTP of the EUO wood. The results shows that the HTP can decrease the hemicellulose

Table 1

Content of cellulose, hemicellulose and lignin of biochars after hydrothermal treatment of the EUO wood, and the BET surface area.

	Cellulose (%)	Hemicellulose (%)	Lignin (%)	S _{BET} ^a (m ² /g)
EUOAC ₀	45.11	23.53	22.05	0.10
EUOAC ₁	47.64	21.83	29.48	1.18
EUOAC ₂	50.81	15.63	32.55	2.69
EUOAC ₃	51.57	10.59	33.21	3.54
EUOAC ₄	52.96	7.91	33.38	3.57
EUOAC ₅	54.20	6.61	34.54	2.48
EUOAC ₆	56.92	4.25	36.17	5.16
EUOAC ₇	58.76	1.84	38.61	5.31

The specific surface area are calculated in P/P₀ pressure range from 0.05 to 0.3.

contents and then increase the content of the cellulose and lignin. The hemicellulose contents was observed with a decrease from 23.53% to 1.84% following HTP temperature increase from 150 to 200 °C. As illustrated in Table 2, the HTP can also result in higher ACs yield from EUO wood than that in absence of HTP at temperature range from 150 to 180 °C. The reason is that the HTP can degrade the hemicellulose and thus result in the increased specific surface area of the biochars (Table 1). The higher specific surface area of the biochars than EUO wood may enhance the access of the activating agent to substrate surface and subsequently increase ACs yield (Rodríguez-Reinoso and Molina-Sabio, 1992). In order to further investigate the effect of the HTP on the properties of the resulted ACs, the pore volume, pore size distribution (PSD) and surface area were evaluated to characterize the porous structure. Fig. 1 plots N₂ adsorption-desorption isotherms and PSD curves of the EUOACs. Similar isotherms for all EUOACs was observed belonging to typical type IV isotherm and hysteresis loop at high P/P₀ range (0.4–0.9), which indicates the existence of rich amount of mesopores (Yin et al., 2016). Based on Table 2, the proportion of the mesopore pore volume is higher than 90% and up to 99% when HTP temperature going up to 200 °C. Furthermore, the PSD curves demonstrate that all EUOACs have narrow PSD with main width range of 2–4 nm, which also implies that no significant difference of PSD was observed for EUOAC_{1–7} when HTP temperatures increased from 150 to 200 °C. For pore width larger than 4 nm, however, the PSD of all EUOACs showed remarkable changes at different HTP temperatures. These results reveal that HTP have significant effect on PSD of the mesopores.

Table 2 lists the surface area and pore volume features of the EUOACs on basis of the N₂ adsorption-desorption isotherms and Brunauer-Emmett-Teller (BET) method. The specific surface area (S_{BET}) of EUOACs enlarges from 1272.38 to 1534.06 m² g^{−1} when HTP temperature increased from 150 to 170 °C, and then decreased to 1284.69 m² g^{−1} when HTP temperature increased further to 200 °C. This indicates that HTP temperature of 170 °C is the turning point on S_{BET} of EUOACs. The reason is that low HTP temperature (< 170 °C) resulted in the removal of the hemicelluloses without damaging the structure of the celluloses and lignin, which can generate the pore canal to favor the extensive access of the activating agent to substrate surface and finally increase the S_{BET} (Rodríguez-Reinoso and Molina-Sabio, 1992). However, the high HTP temperature (> 170 °C) caused the collapse of the substrate structure and prevented the activating agent from extensive access to the substrate surface. Furthermore, both S_{micro} and V_{micro} show similar development as S_{BET} when HTP temperature increased from 150 to 200 °C. At 170 °C, S_{micro} and V_{micro} separately reached the highest values of 582.76 m² g^{−1} and 0.31 cm³ g^{−1} (for EUOAC₃), whereas EUOAC₃ had lowest S_{meso} of 951.30 m² g^{−1} and V_{meso} of 0.98 cm³ g^{−1} compared to other EUOACs. All EUOACs had much higher S_{meso} and V_{meso} than S_{micro} and V_{micro}, respectively, which is coincident with the observation in Fig. 1 that EUOACs are mainly in mesoporous range. The morphological features analyzed by SEM (Fig. S1) also illustrate that EUOACs are rich in porous structure. On the other hand, EUOAC₄ was observed with highest V_{total} (1.78 cm³ g^{−1}), V_{meso} (1.66 cm³ g^{−1}), D_{total}

Table 2
Pore characteristics and the yield of EUOACs.

Substrates	S_{BET}^a (m^2g^{-1})	S_{micro}^b (m^2g^{-1})	S_{meso}^c (m^2g^{-1})	V_{total}^d (cm^3g^{-1})	V_{micro}^e (cm^3g^{-1})	V_{meso}^f (cm^3g^{-1})	D_{total}^g (nm)	D_{meso}^h (nm)	Yield ⁱ (%)
EUOAC ₀	1405.43	243.65	1161.78	1.31	0.13	1.18	3.32	3.89	38.16
EUOAC ₁	1272.38	63.25	1209.13	1.39	0.03	1.36	4.38	4.91	41.88
EUOAC ₂	1498.85	253.31	1245.54	1.79	0.12	1.66	4.77	5.90	42.05
EUOAC ₃	1534.06	582.76	951.30	1.29	0.31	0.98	3.36	4.24	40.72
EUOAC ₄	1456.69	245.80	1210.89	1.78	0.12	1.66	4.89	6.02	39.20
EUOAC ₅	1420.18	165.77	1254.41	1.53	0.08	1.45	4.71	5.35	39.96
EUOAC ₆	1393.82	92.23	1301.59	1.53	0.04	1.49	4.30	5.07	34.87
EUOAC ₇	1284.69	33.68	1251.01	1.51	0.01	1.50	4.39	5.28	36.74

^a Specific surface area calculated in P/P₀ pressure range from 0.05 to 0.3.

^b Micropore surface area calculated from t-plot method.

^c Mesopore surface area calculated from t-plot method.

^d Total pore volume (V_{total}) at P/P₀ = 0.95.

^e Microproe pore volume (V_{micro}) calculated from t-plot method.

^f $V_{\text{meso}} = V_{\text{total}} - V_{\text{micro}}$.

^g Average pore diameter of total pore.

^h Average pore diameter of mesopore.

ⁱ Activated carbon yield was calculated based on dry weight of EUO wood.

(4.89 nm) and D_{meso} (6.02 nm) values among all the EUOACs, and EUOAC₆ had highest S_{meso} of 1301.59 m^2g^{-1} . The variations in surface area, pore volume and pore width could be attributed to the substrate composition development influenced by HTP (Zhu et al., 2017) and pore formation concept of H_3PO_4 activation (Danish et al., 2014a, 2014b). As for electrode material application in supercapacitor, the EUOACs with large S_{BET} and composite structure of micropore and mesopore can be potential candidate for better capacitance performance. As the consequence, the capacitive behavior of all EUOACs will be studied in detail through CV, EIS, GCD and cycling analysis.

3.2. Element analysis and surface chemistry characterization

Table 3 describes the elemental composition of the EUOACs analyzed by using CHNS analysis. Limited contents of S and N were detected in all samples with proportion lower than 0.3%. The element of C was observed with a sharp increase from 65.13% to 75.54%, whereas the elements of O and H go through a decrease as HTP temperature increased from 150 to 200 °C. This phenomena indicates that the increase of HTP temperature can improve the C content of the EUOACs. As shown in Table 1, the hemicellulose content decreased as HTP temperature increase from 150 to 200 °C. Considering that the hemicellulose is rich in O– and H– groups, the removal of hemicellulose during HTP can result in the increase of C content and decrease of the O

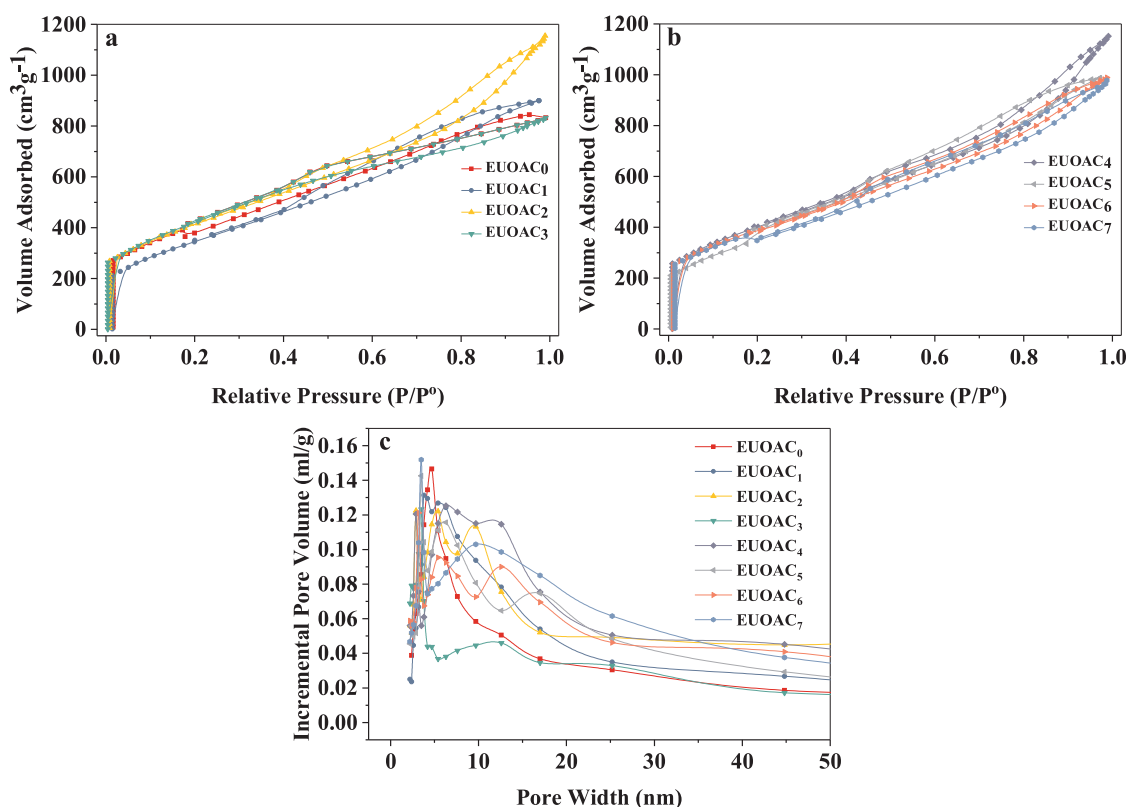


Fig. 1. N₂ adsorption-desorption isotherm for EUOAC₀₋₃ (a) and EUOAC₄₋₇ (b); the pore size distribution (c) for the EUOACs.

Table 3
Elemental compositions of EUOACs.

Element (%)	EUOAC ₀	EUOAC ₁	EUOAC ₂	EUOAC ₃	EUOAC ₄	EUOAC ₅	EUOAC ₆	EUOAC ₇
C	65.13	70.86	70.42	70.43	74.41	73.39	76.87	75.54
O	31.39	25.64	26.13	26.33	22.35	23.29	20.07	21.46
H	3.06	2.92	2.95	2.87	2.85	2.81	2.62	2.63
N	0.25	0.31	0.22	0.17	0.20	0.29	0.26	0.26
S	0.17	0.27	0.28	0.21	0.20	0.22	0.17	0.11

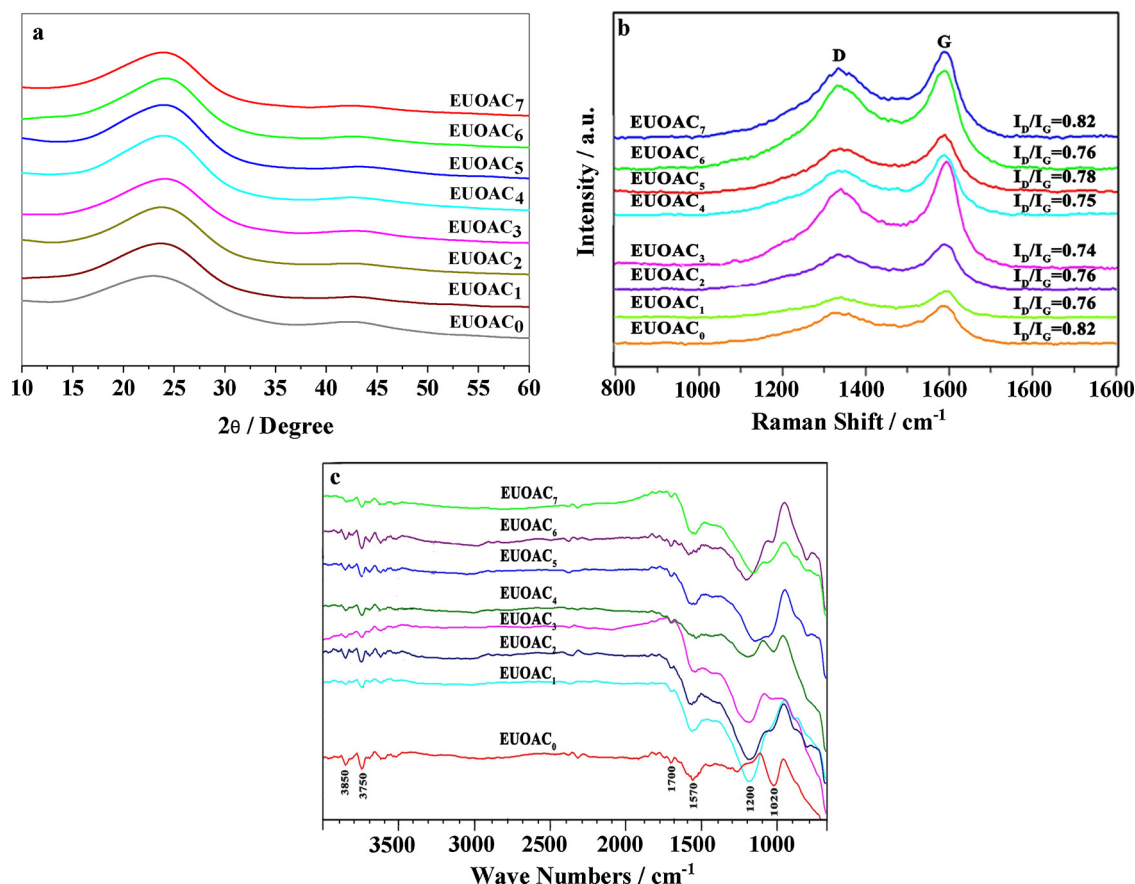


Fig. 2. XRD pattern (a), Raman spectra (b) and RT-IR spectra (c) of the EUOACs.

and H content of the EUOACs after activation. These results proved that the HTP can significantly influence the elemental composition of EUOACs during the process of the carbonization and activation of the EUOACs.

The XRD patterns of all EUOACs are presented in Fig. 2a. Two broad peaks were observed around 23° and 43°, which are corresponding to (002) and (100) planes of carbon, respectively (Karnan et al., 2017). This indicates that all EUOACs had similar nature of crystallinity. The similar results were also reported by Karnan et al., (2017) in corncob derived ACs. Raman spectroscopy is usually applied to analyze the extent of functionalization in biomass-derived ACs. As shown in Fig. 2b, the I_D/I_G ratio indicates the degree of defective nature and graphitization of the EUOACs after carbonization and activation of the biochar samples. A typical D and G bands were observed in all EUOACs at 1320 and 1590 cm^{-1} , respectively. The variation of the I_D/I_G ratio in EUOACs implies that the different HTP temperatures can result in the changes of the graphitization degree in EUOACs. EUOAC₃ gained lowest I_D/I_G ratio of 0.74, which demonstrates that highest degree of graphitization (Karnan et al., 2017) was achieved at HTP temperature of 170 °C. The decomposition of the hemicellulose at 170 °C during HTP generates the optimal pore canal with highest surface area (Table 1).

The higher surface area may help the activation agent to get higher chance to access the substrate surface and then result in higher degree of graphitization (Rodríguez-Reinoso and Molina-Sabio, 1992). Fig. 2c presents FT-IR spectra of all EUOACs with wave number from 400 to 4000 cm^{-1} . The O–H stretching vibration located around 3750 and 3850 cm^{-1} may attribute to the chemisorbed H_2O and hydroxyl group on the EUOACs. C=C stretching vibration was observed around 1570 m^{-1} and may be assigned to the typical olefinic group (Karnan et al., 2017). EUOAC₄ was observed with much lower vibrational amplitude, which implies that the graphitization is largely enhanced at HTP temperature of 170 °C. This observation is coincident to the phenomenon observed in Raman spectrum. The peaks located at around 1200 and 1020 cm^{-1} may belong to C–O stretching vibration (Yin et al., 2016). The C–O stretching location for EUOAC₀ was shifted from 1200 and 1020 cm^{-1} comparing with EUOAC_{1–7} it indicates that the HTP may affect the C–O stretching modes. To sum up, the CHNS, XRD, Raman and FTIR characterization prove that HTP effectively influenced the elemental composition and surface chemistry characteristics of the EUOACs by manipulating the substrate structure of the ACs precursor.

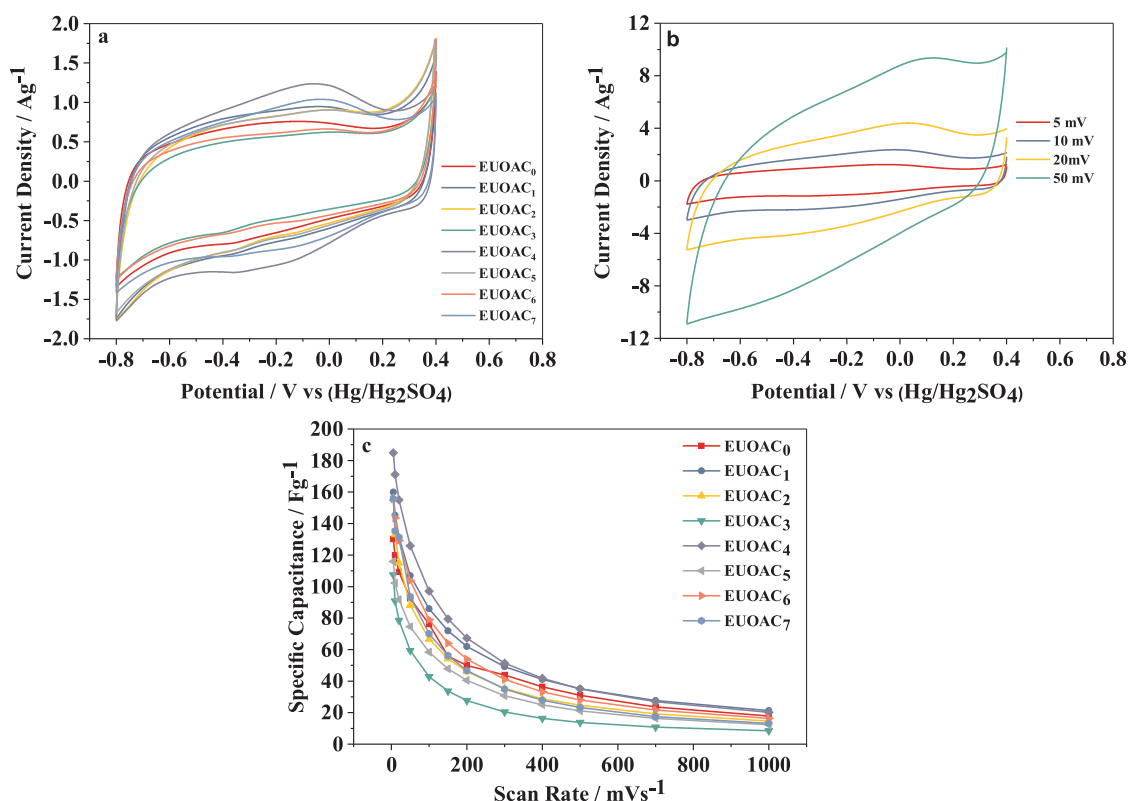


Fig. 3. CV curves of EUOACs electrodes at scan rate of 5 mV/s in 1 M H₂SO₄ aqueous solutions (a); CV curves of EUOAC₄ electrode at various scan rates (b); calculated specific capacitance from CV curves at various scan rates (c).

3.3. Electrochemical studies

3.3.1. Cyclic voltammetry (CV) analysis

Cyclic voltammetry (CV) has been frequently applied to evaluate the electrochemical behavior of electrode materials for supercapacitors. The CV curves of all EUOACs are displayed in Fig. S2 at various scan rates ranging from 5 to 1000 mVs⁻¹. All the CVs were analyzed in the three-electrode system using 1 M H₂SO₄ as electrolyte, and the potential window ranged from -0.8 to 0.4 V vs (Hg/Hg₂SO₄). The EUOACs, Hg/Hg₂SO₄ electrode and platinum plate were used as working electrode, counter electrode and reference electrode, respectively. Fig. 3a depicts the CVs at scan rate of 5 mVs⁻¹, presenting the capacitive performance of the all EUOACs. It can be clearly observed that the EUOAC₄ displays the electrical double layer capacitance (EDLC) like behavior with distinct pseudocapacitive characteristic. The best charge-discharge performance of EUOAC₄ mainly attribute to EDLC that caused by its large S_{BET} and well-developed composite structure of micropores and mesopores, and the pseudocapacitance effect may be caused by the certain amount of the oxygen-based functional groups. The presence of the EDLC like behavior along with pseudocapacitance effect in EUOAC₄ can be clearly seen in CV curves at various scan rates from 5 to 50 mVs⁻¹ (Fig. 3b). As illustrated in Fig. 3c, the specific capacitance (SC) was calculated from the CV profiles in Fig. S2 by using Eq. (1). The SC values of all EUOACs become lower with increasing scan rates. The maximum SC value of 185 Fg⁻¹ was obtained for EUOAC₄ at the lowest scan rate of 5 mVs⁻¹, whereas EUOAC₃ gained the lowest SC of 107 Fg⁻¹. The EUOAC₁, EUOAC₂, EUOAC₅ and EUOAC₆ also demonstrate better rate performance because of their larger pore size than EUOAC₀, EUOAC₃ and EUOAC₇. The above data analysis regarding to CVs profile shape and SC are in great agreement with the results obtained with N₂ adsorption-desorption isotherm, XRD, Raman and FTIR measurements. In summary, the CV profiles and calculated SC data demonstrate that EUO-derived activated carbons present desirable EDLC performance in aqueous H₂SO₄ electrolyte along with significant pseudocapacitance.

3.3.2. Electrochemical impedance spectroscopy analysis

Electrochemical impedance spectroscopy (EIS) technique was also carried out to further investigate the electrochemical impedance of the charge transfer, ion diffusion and capacitive features. The Nyquist plots for all EUOACs are shown in Fig. 4a, where the frequency range used for the EIS tests is from 100 kHz to 10 mHz. The intercept of the Nyquist plots with horizontal axis is referred as the equivalent series resistance (ESR), which is collective contribution from intrinsic electrode resistance and contact resistance between electrode and current collector. The ESR for all EUOACs are lower than 0.5 Ω . The EIS spectra of the EUOACs can be divided into three portions including low-frequency range (< 0.1 Hz), middle-frequency range (from 0.1 to 10 Hz) and high-frequency range (> 10 Hz). In the low-frequency region, the line with good linearity for all EUOACs indicate typically capacitive characteristics due to the formation of the charge-discharge performance of the EDLC on the surface of the porous structure. As a transitional zone (known as “knee”) between the low-frequency range and high frequency-range, the middle frequency region demonstrate a shift from capacitive behavior to resistive behavior. Furthermore, the slope of the impedance curves of all EUOACs in middle-frequency range approaches 45°, which indicate the ion diffusion into the pores on electrode-electrolyte interface. The maximum frequency at “knee” is corresponding to the “knee frequency”, which indicate the rate performance for a supercapacitor because it is closely linked to the porous structure of the EUOACs (Yin et al., 2016). As plotted in Fig. 4a, the similar “knee frequency” of EUOAC₂ and EUOAC₄ implies their similar porous structure. This evidence is also confirmed by the results shown in Table 3. The high-frequency range is also known as Warburg range, in which the impedance curves usually form a semicircle indicating the inner resistance of electrode. The distinct difference of the semicircle diameter illustrates the variation of the inner resistance of the EUOACs electrode.

Fig. 4b and c illustrate the real and imaginary capacitance development respectively versus frequency for all EUOACs, respectively. The

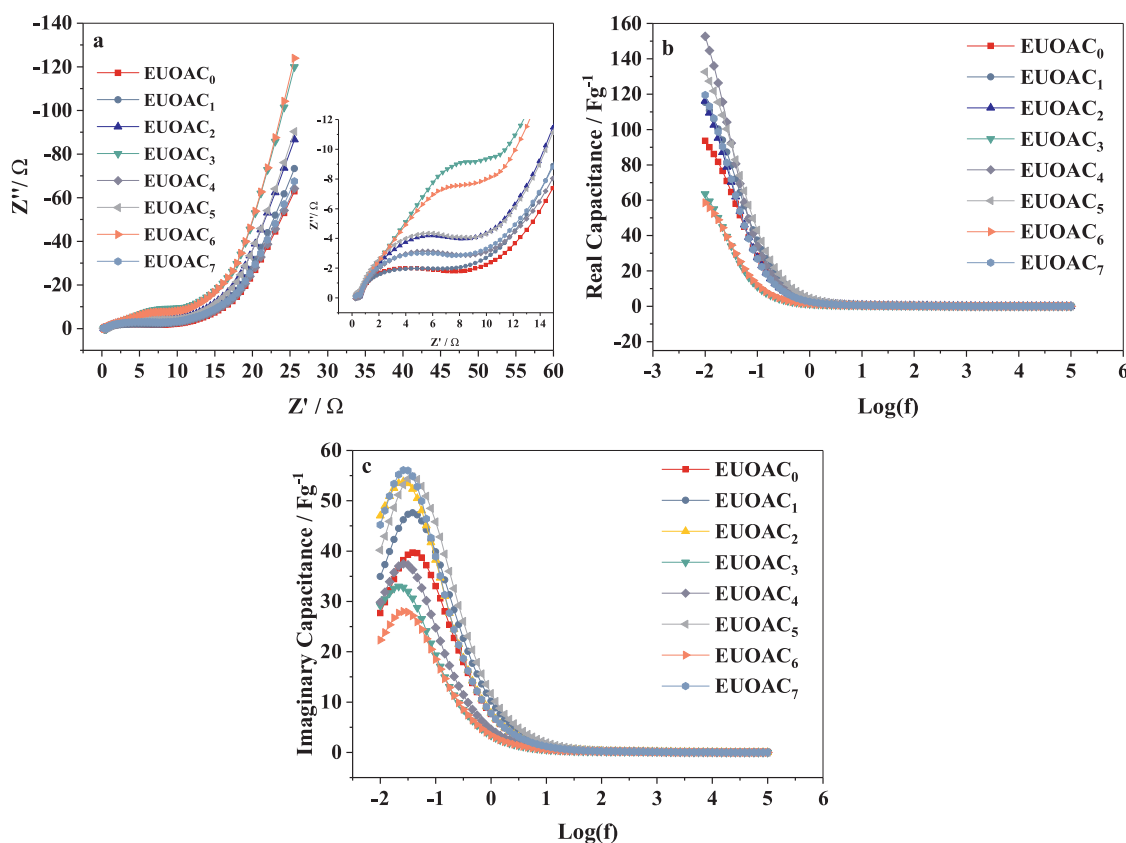


Fig. 4. EIS spectrum for EUOACs electrodes (a); curves for real capacitance versus impedance frequency (b); curves for imaginary capacitance versus impedance frequency (c); curves for specific capacitance versus impedance frequency (d).

capacitance of real part (C') was observed with maximum value at the lowest frequency, indicating the capacitance saturation that the electrolyte ions deeply penetrate into the pores of the electrode materials and form a high capacitance value. From Fig. 4b, it can be observed that EUOAC₄ have higher capacitance of 153 Fg^{-1} than other samples, and EUOAC₇ gain lowest capacitance of 58 Fg^{-1} . These results are in coherence with the data of CV test. However, C' decrease sharply with the increase in frequency in the range of $0.01\text{--}0.1 \text{ Hz}$ and become steady above 10 Hz , suggesting that the electrolyte has limited access to penetration into the porous materials at higher frequency and lead to the rapid decline of the C' . In Fig. 4c, a maximum capacitance of imaginary part (C'') was observed at frequency of f_0 which is corresponding to a relaxation time τ° ($\tau^\circ = 1/f_0$). The τ° is considered as the badly-needed minimum time for the capacitor to release all energy with an efficiency of above 50%, manifesting the maximum accessibility of electrolyte ions to the outside surface of the electrode active materials (Pech et al., 2010). The τ° for all EUOACs are 26.1 s, 26.1 s, 38.3 s, 46.4 s, 38.3 s, 38.3 s, 26.1 s and 38.3 s, respectively. The longest relaxation time for EUOAC₃ might be attributed to its lower S_{meso} , V_{meso} , and D_{meso} than other samples as shown in Table 2. The results imply that higher mesopore surface area and larger mesopore diameter can result in good contact between electrode and electrolyte.

3.3.3. Charge-discharge studies

Fig. 5a presents the GCD profiles of all EUOACs in acid electrolyte at current density of 0.2 Ag^{-1} . The charge-discharge curves shows linear and symmetrical behavior, indicating the excellent capacitive features. There is an evident internal resistance (IR) drop was observed on the initiation point of the discharge curves. The IR drop is associated to the conductivity and porous structure of the electrode active materials (Sun et al., 2016). EUOAC₃ gained largest IR drop (0.033 V), while the IR drop for EUOAC₄ is only 0.02 V . The may be attributed to the higher

conductivity of EUOAC₄ indicated with the higher degree of graphitization in Raman spectrum and lower vibrational amplitude in FTIR spectrum. The much higher S_{meso} , V_{meso} and D_{meso} values of EUOAC₄ than EUOAC₃ (Table 2) may also contribute to the lower IR drop due to fact that the large fraction of the mesopores can result in less resistance of the electrolyte ion migration than micropores at same current density (Karnan et al., 2017). Fig. 5b displays the distinct charge-discharge time spans of EUOAC₄ at various current density, the lower current density led to the longer charge-discharge time span. The IR drop also went through an increase from 0.02 to 0.1 V as current density increased, indicating a decline of the discharge capacitance (DC) versus current density as shown in Fig. 5c. Fig. S3 illustrates the GCD behavior of all EUOACs at various current density ($0.2, 0.5, 0.7, 1.2$ and 2 Ag^{-1}). On the basis of the GCD curves in Fig. S3, the DC was calculated from the linear parts of the discharge curve after IR drop by using Eq. (4). Fig. 5c depicts the DC development versus current density. It is clearly observed that the DC curves have a notable decrease with the increasing current density from 0.2 to 2.0 Ag^{-1} . This tendency is also coincident to the increase of IR drop. This can be explained by the fact that the low charging rate can enhance the ion diffusion to the both micro- and meso- porous structure and high charging rate result in limited access of the electrolyte ions into the mesoporous structure. The DC retention in Fig. 5c were around 78%, 75%, 66%, 69%, 70%, 73%, 75% and 69% for EUOAC₀, EUOAC₁, EUOAC₂, EUOAC₃, EUOAC₄, EUOAC₅, EUOAC₆ and EUOAC₇, respectively, when the current density increased from 0.2 to 2 Ag^{-1} . EUOAC₄ shows highest DC of 158 Fg^{-1} at 0.2 Ag^{-1} and reduce to 111 Fg^{-1} at 2 Ag^{-1} , whereas EUOAC₃ get lowest DC of 75 Fg^{-1} and reduce to 69 Fg^{-1} . This result is well agreed with CV results. Such phenomenon could be attributed to the fact that the porous structure of active materials with large fraction of the mesopores lead to the higher accessibility for electrolyte ions to electrode surface, resulting in high capacitance.

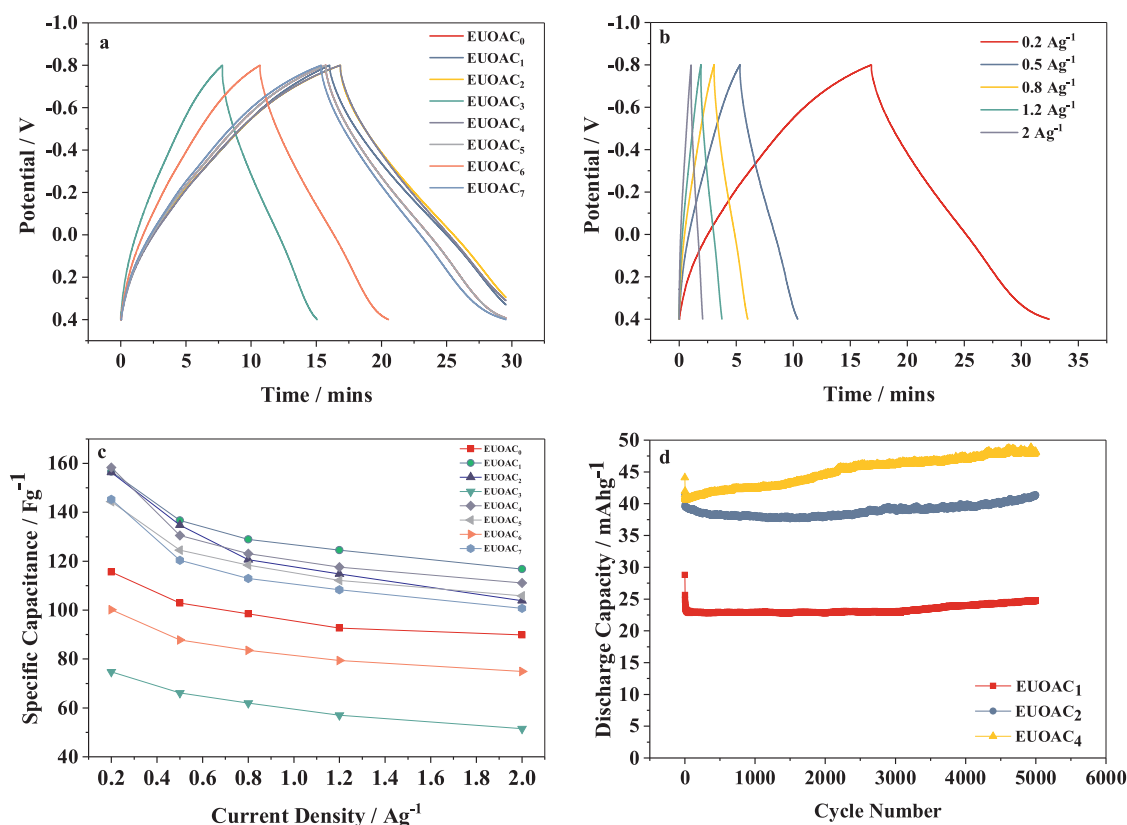


Fig. 5. GCD curves of EUOACs electrodes at current density of 200 mA g⁻¹ (a); GCD curves of EUOAC₄ electrode at various current density (b); the discharge capacity calculated from GCD curves at various current density (c); the long cycling performance of EUOACs electrodes at current density of 1 A g⁻¹ (d).

3.3.4. Cycling studies

The long-term cycling performance for EUOAC₁, EUOAC₂ and EUOAC₄ electrodes was investigated for 5000 cycles at the current density of 1 A g⁻¹ (Fig. 5d). It was observed that a remarkable decline of the discharge capacitance on initial stage and thereafter the discharge capacitance become stabilized. The discharge capacitance loss for EUOAC₁, EUOAC₂ and EUOAC₄ are 10.5%, 8.1% and 4.7%, respectively, after 1000 cycles of continuous charge-discharge. After operating of 5000 cycles, the capacity retention of EUOAC₁, EUOAC₂ and EUOAC₄ are respectively 94%, 96% and 93%, implying that the EUO derived porous carbon materials manifest satisfying long-term stability. Though, EUOAC₂ might be a better candidate electrode materials for supercapacitor application according to the cycling test, the stability is not much improved compare to EUOAC₄. EUOAC₄ gain higher average discharge capacitance (86 mAhg⁻¹) than EUOAC₁ (25 mAhg⁻¹) and EUOAC₂ (47 mAhg⁻¹) after long-term continuous charge-discharge processing. Therefore, the above experiments clearly confirm that EUOAC₄ electrode is the optimum materials for supercapacitor application. The EUO wood derived activate carbon produced through hydrothermal pretreatment and followed by low-temperature chemical activation makes the EUO wood for feasible application in supercapacitors.

4. Conclusion

The EUO wood derived activated carbons have been intensively characterized as electrode materials for supercapacitors application. The HTP followed by low-temperature chemical activation of EUO wood resulted in the formation of the amorphous carbon with composite structure of micropores and mesopores. Based on specific surface area, the ratio of mesopores to micropores ranged from 1.6 to 37.1, whereas the ratio based on pore volume was in range of 3.2–150.0. However, the optimal ratio for high capacitive performance were 4.9

and 13.8 for calculation based on specific surface area and pore volume, respectively. The characterization of the porous structure and capacitive behavior revealed that higher mesopore surface area (1456.09 m² g⁻¹), mesopore pore volume (1.66 cm³ g⁻¹) and larger mesopore diameter (6.02 nm) can generate higher specific capacitance due to the excessive contact between electrode and electrolyte. The EUOACs performed specific capacitance as high as 185 Fg⁻¹ and satisfied long-term stability, which proves that the EUO wood are viable for supercapacitors application.

Acknowledgments

This research was supported by China Postdoctoral Science Foundation (2017M61325), the “PhD Start-up” Funds of Northwest A&F University (2452016159) and the Fundamental Research Funds for the Central Universities (2452017129).

Appendix A. Supplementary data

Supplementary material related to this article can be found, in the online version, at doi:<https://doi.org/10.1016/j.indcrop.2018.08.082>.

References

- Ahmad, T., Danish, M., 2018. Prospects of banana waste utilization in wastewater treatment: a review. *J. Environ. Manage.* 206, 330–348.
- Barzegar, F., Bello, A., Dangbegnon, J.K., Manyala, N., Xia, X., 2017. Asymmetric carbon supercapacitor with activated expanded graphite as cathode and pinecone tree activated carbon as anode materials. *Energy Procedia* 105, 4098–4103.
- Beidaghi, M., Gogotsi, Y., 2014. Capacitive energy storage in micro-scale devices: recent advances in design and fabrication of micro-supercapacitors. *Energy Environ. Sci.* 7, 867.
- Borenstein, A., Hanna, O., Attias, R., Lusk, S., Brousse, T., Aurbach, D., 2017. Carbon-based composite materials for supercapacitor electrodes: a review. *J. Mater. Chem. A* 5, 12653–12672.

- Bouchelta, C., Medjram, M.S., Bertrand, O., Bellat, J.P., 2008. Preparation and characterization of activated carbon from date stones by physical activation with steam. *J. Anal. Appl. Pyrolysis* 82, 70–77.
- Boyjoo, Y., Cheng, Y., Zhong, H., Tian, H., Pan, J., Pareek, V.K., Jiang, S.P., Lamonier, J.F., Jaroniec, M., Liu, J., 2017. From waste Coca Cola® to activated carbons with impressive capabilities for CO₂ adsorption and supercapacitors. *Carbon N. Y.* 116, 490–499.
- Chiam, S.L., Lim, H.N., Foo, C.Y., Pandikumar, A., Huang, N.M., 2017. How did nickel cobaltite reinforced carbon microfibre symmetrical supercapacitor fare against a commercial supercapacitor? *Electrochim. Acta* 246, 1141–1146.
- Danish, M., Hashim, R., Ibrahim, M.N.M., Sulaiman, O., 2014a. Optimized preparation for large surface area activated carbon from date (*Phoenix dactylifera* L.) stone biomass. *Biomass Bioenergy* 61, 167–178.
- Danish, M., Hashim, R., Ibrahim, M.N.M., Sulaiman, O., 2014b. Optimization study for preparation of activated carbon from Acacia mangium wood using phosphoric acid. *Wood Sci. Technol.* 48, 1069–1083.
- Danish, M., Khanday, W.A., Hashim, R., Sulaiman, N.S.B., Akhtar, M.N., Nizami, M., 2017. Application of optimized large surface area date stone (*Phoenix dactylifera*) activated carbon for rhodamin B removal from aqueous solution: Box-Behnken design approach. *Ecotoxicol. Environ. Saf.* 139, 280–290.
- Gao, F., Qu, J., Zhao, Z., Wang, Z., Qiu, J., 2016. Nitrogen-doped activated carbon derived from prawn shells for high-performance supercapacitors. *Electrochim. Acta* 190, 1134–1141.
- Guo, Y., Rockstraw, D.A., 2006. Physical and chemical properties of carbons synthesized from xylan, cellulose, and Kraft lignin by H₃PO₄ activation. *Carbon N. Y.* 44, 1464–1475.
- Hao, W., Björnerbäck, F., Trushkina, Y., Bengoechea, M.O., Salazar-Alvarez, G., Barth, T., Hedin, N., 2017. High-performance magnetic activated carbon from solid waste from lignin conversion processes. Part I: their use as adsorbents for CO₂. *Energy Procedia* 114, 6272–6296.
- Jain, A., Balasubramanian, R., Srinivasan, M.P., 2015. Production of high surface area mesoporous activated carbons from waste biomass using hydrogen peroxide-mediated hydrothermal treatment for adsorption applications. *Chem. Eng. J.* 273, 622–629.
- Ji, Z., Su, Y., 2006. Effects of planting modes on secondary metabolite contents in *Eucommia ulmoides* barks. *Acta Bot. Boreali-Occident. Sin.* 26, 1911–1915.
- Karnan, M., Subramani, K., Srividhya, P.K., Sathish, M., 2017. Electrochemical studies on corncob derived activated porous carbon for supercapacitors application in aqueous and non-aqueous electrolytes. *Electrochim. Acta* 228, 586–596.
- Lee, M.S., Choi, H.J., Baek, J.B., Chang, D.W., 2017. Simple solution-based synthesis of pyridinic-rich nitrogen-doped graphene nanoplatelets for supercapacitors. *Appl. Energy* 195, 1071–1078.
- Li, B., Dai, F., Xiao, Q., Yang, L., Shen, J., Zhang, C., Cai, M., 2016. Nitrogen-doped activated carbon for a high energy hybrid supercapacitor. *Energy Environ. Sci.* 9, 102–106.
- Liu, X., Li, S., Mi, R., Mei, J., Liu, L.M., Cao, L., Lau, W.M., Liu, H., 2015. Porous structure design of carbon xerogels for advanced supercapacitor. *Appl. Energy* 153, 32–40.
- Ma, G., Yang, Q., Sun, K., Peng, H., Ran, F., Zhao, X., Lei, Z., 2015. Nitrogen-doped porous carbon derived from biomass waste for high-performance supercapacitor. *Bioresour. Technol.* 197, 137–142.
- Ohno, H., Fukumoto, K., 2008. Progress in ionic liquids for electrochemical reaction matrices. *Electrochemistry* 76, 16–23.
- Pech, D., Brunet, M., Durou, H., Huang, P., Mochalin, V., Gogotsi, Y., Taberna, P., Simon, P., 2010. Ultrahigh-power micrometre-sized supercapacitors based on onion-like carbon. *Nat. Nanotechnol.* 5, 651–654.
- Potphode, D.D., Mishra, S.P., Sivaraman, P., Patri, M., 2017. Asymmetric supercapacitor devices based on dendritic conducting polymer and activated carbon. *Electrochim. Acta* 230, 29–38.
- Redondo, E., Carretero-González, J., Goikolea, E., Ségolini, J., Mysyk, R., 2015. Effect of pore texture on performance of activated carbon supercapacitor electrodes derived from olive pits. *Electrochim. Acta* 160, 178–184.
- Rodríguez-Reinoso, F., Molina-Sabio, M., 1992. Activated carbons from lignocellulosic materials by chemical and/or physical activation: an overview. *Carbon N. Y.* 30, 1111–1118.
- Sodtipinta, J., Jeosakulrat, C., Poonyayant, N., Kidkhunthod, P., Chanlek, N., Amornsakchai, T., Pakawatpanurut, P., 2017. Interconnected open-channel carbon nanosheets derived from pineapple leaf fiber as a sustainable active material for supercapacitors. *Ind. Crops Prod.* 104, 13–20.
- Stoller, M.D., Ruoff, R.S., 2010. Best practice methods for determining an electrode material's performance for ultracapacitors. *Energy Environ. Sci.* 3, 1294.
- Sun, W., Lipka, S.M., Swartz, C., Williams, D., Yang, F., 2016. Hemp-derived activated carbons for supercapacitors. *Carbon N. Y.* 103, 181–192.
- Tan, X. fei, Liu, S. bo, Liu, Y. guo, Gu, Y. ling, Zeng, G. ming, Hu, X. jiang, Wang, X., Liu, S. heng, Jiang, L. hua, 2017. Biochar as potential sustainable precursors for activated carbon production: multiple applications in environmental protection and energy storage. *Bioresour. Technol.* 227, 359–372.
- Tang, Z., Pei, Z., Wang, Z., Li, H., Zeng, J., Ruan, Z., Huang, Y., Zhu, M., Xue, Q., Yu, J., Zhi, C., 2018. Highly anisotropic, multichannel wood carbon with optimized heteroatom doping for supercapacitor and oxygen reduction reaction. *Carbon N. Y.* 130, 532–543.
- Teng, Y., Liu, E., Ding, R., Liu, K., Liu, R., Wang, L., Yang, Z., Jiang, H., 2016. Bean dregs-based activated carbon/copper ion supercapacitors. *Electrochim. Acta* 194, 394–404.
- Tian, X., Ma, H., Li, Z., Yan, S., Ma, L., Yu, F., Wang, G., Guo, X., Ma, Y., Wong, C., 2017. Flute type micropores activated carbon from cotton stalk for high performance supercapacitors. *J. Power Sources* 359, 88–96.
- Wang, B., Qiu, J., Feng, H., Sakai, E., Komiya, T., 2016. KOH-activated nitrogen doped porous carbon nanowires with superior performance in supercapacitors. *Electrochim. Acta* 190, 229–239.
- Xiao, P.W., Zhao, L., Sui, Z.Y., Xu, M.Y., Han, B.H., 2017. Direct synthesis of ordered mesoporous hydrothermal carbon materials via a modified soft-templating method. *Microporous Mesoporous Mater.* 253, 215–222.
- Yagmur, E., Tunc, M.S., Banford, A., Aktas, Z., 2013. Preparation of activated carbon from autohydrolysed mixed southern hardwood. *J. Anal. Appl. Pyrolysis* 104, 470–478.
- Yang, J., Wang, Y., Luo, J., Chen, L., 2018. Highly nitrogen-doped graphitic carbon fibers from sustainable plant protein for supercapacitor. *Ind. Crops Prod.* 121, 226–235.
- Yin, J., Zhu, Y., Yue, X., Wang, L., Zhu, H., Wang, C., 2016. From environmental pollutant to activated carbons for high-performance supercapacitors. *Electrochim. Acta* 201, 96–105.
- Yu, A., Chen, Z., Maric, R., Zhang, L., Zhang, J., Yan, J., 2015. Electrochemical supercapacitors for energy storage and delivery: advanced materials, technologies and applications. *Appl. Energy* 153, 1–2.
- Zhang, Y., Gao, Z., Song, N., Li, X., 2016. High-performance supercapacitors and batteries derived from activated banana-peel with porous structures. *Electrochim. Acta* 222, 1257–1266.
- Zhang, W., Lin, N., Liu, D., Xu, J., Sha, J., Yin, J., Tan, X., Yang, H., Lu, H., Lin, H., 2017. Direct carbonization of rice husk to prepare porous carbon for supercapacitor applications. *Energy* 128, 618–625.
- Zhu, M.Q., Wang, Z.W., Wen, J.L., Qiu, L., Zhu, Y.H., Su, Y.Q., Wei, Q., Sun, R.C., 2017. The effects of autohydrolysis pretreatment on the structural characteristics, adsorptive and catalytic properties of the activated carbon prepared from *Eucommia ulmoides* Oliver based on a biorefinery process. *Bioresour. Technol.* 232, 159–167.
- Zhuo, H., Hu, Y., Tong, X., Zhong, L., Peng, X., Sun, R., 2016. Sustainable hierarchical porous carbon aerogel from cellulose for high-performance supercapacitor and CO₂ capture. *Ind. Crops Prod.* 87, 229–235.